Tunnelling and Underground Space Technology 77 (2018) 13–25

Contents lists available at ScienceDirect

Tunnelling and Underground Space Technology

journal homepage: www.elsevier.com/locate/tust

Analytical and experimental evaluation of the use of fibers as partial reinforcement in shotcrete for tunnels in Chile

Leonardo M. Massone*, Francisco Nazar

Department of Civil Engineering, University of Chile, Blanco Encalada 2002, Santiago, Chile

ARTICLE INFO

Keywords:
Tunnel
Shotcrete
Fiber reinforced concrete
Seismic response
Steel fiber
Polypropylene fiber

ABSTRACT

This work evaluates experimentally the use of steel or polypropylene fibers in shotcrete as a partial replacement for the traditional reinforcement of electrowelded mesh used at the tunnel support for the subway in Santiago (Chile). For the experimental part, 8 tests were performed on section-scaled (1:2) slender (half-span to depth ratio a/d ~ 5) specimens under transversal (flexure and shear) and axial loads ($0.02f'_cA_g$ and $0.07f'_cA_g$) and with different reinforcements layout; and another 4 tests of similar specimens, but with low half-span to depth ratio (a/d ~ 1.5). The section includes welded mesh (one face), a central reticulated frame and a plane shotcrete with a welded mesh (opposite face) or reinforced shotcrete (steel or polypropylene). The results showed a very important contribution of the reticulated frame in flexion (main internal reinforcement) and a modest contribution of the welded mesh and fibers. A two-dimensional finite element modeling of the tunnel-ground system using OpenSees is also performed using calibrated models for the tunnel section based on the experimental part. The soil is modeled with 9-node quadrilateral elements, the lining is modeled with beam-column elements with fiber sections, and the interaction between the lining and the soil is modeled by the Winkler approach without tension in the direction normal to the contact surface and with perfect adherence in the tangential direction. The model is subjected to the static loads from the excavation, modeled considering the constructive sequence of the tunnel using the α method, and then to a seismic analysis by means of the shear wave method (distortion). The results show that the safety factors implicit in the traditional design are high, implying that the structure remains elastic.

1. Introduction

A tunnel is an underground passageway dug through the surrounding rock or soil, which is used to enable passage for vehicles, people, or water. The material surrounding the tunnel depends on the terrain conditions. In rock, for example, there may be no need for any support to be sustained, and structural stability is entirely dependent on the rock itself. In materials of lower self-supporting capacity, such as soil, it is necessary to incorporate some additional structure that supports the material, and since tunnels usually require their interior with open access, the use of linings that act as arches (together with the soil's own self-support capacity) is the preferred solution.

The structural design should consider the bending induced on the lining. Estimating the bending stresses induced on the tunnel support is complex, because it is difficult to estimate how the loads are distributed between the lining and the soil, as well as the earthquake-induced loads. The literature recognizes three different systems of commonly used concrete tunnel linings: (i) prefabricated segment linings; (ii) projected (shotcrete) concrete linings; and (iii) in-situ concrete linings. Other support measures are reticulated frames, glass fiber bolts, and longitudinal umbrellas, among others. The first system consists of prefabricating curved segments and joining them together by being seated in the ground. The second consists of shotcreting against the ground and other supporting elements, such as meshes, reticulated frames, bolts, etc. The last system consists of concreting in a traditional way, with moldings, and could be combined with the second method. Nowadays, thanks to the proliferation of the New Austrian Tunneling Method (NATM), the use of shotcrete for the lining has become more widespread (Kolymbas, 2005). The shotcrete is typically reinforced with electrowelded meshes, and in recent times discrete fibers have been used as replacement of steel mesh, using what is traditionally known as fiber reinforced concrete (FRC). FRC is a material made with hydraulic cement, aggregates of various sizes, incorporating discrete, discontinuous fibers (Bentur and Mindess, 2006). FRC is attributed great benefits, both structural and non-structural. Examples of the first are: (i) greater ductility; (ii) better cracking control; (iii) better flexural behavior; and (iv) residual tensile strength, among others. Examples of the second ones are: (i) a better performance in the case of freeze-thaw

* Corresponding author.
E-mail addresses: lmassone@ing.uchile.cl (L.M. Massone), francisco.nazar@ing.uchile.cl (F. Nazar).

https://doi.org/10.1016/j.tust.2018.03.027
Received 4 September 2017; Received in revised form 20 March 2018; Accepted 24 March 2018
Available online 28 March 2018
0886-7798/

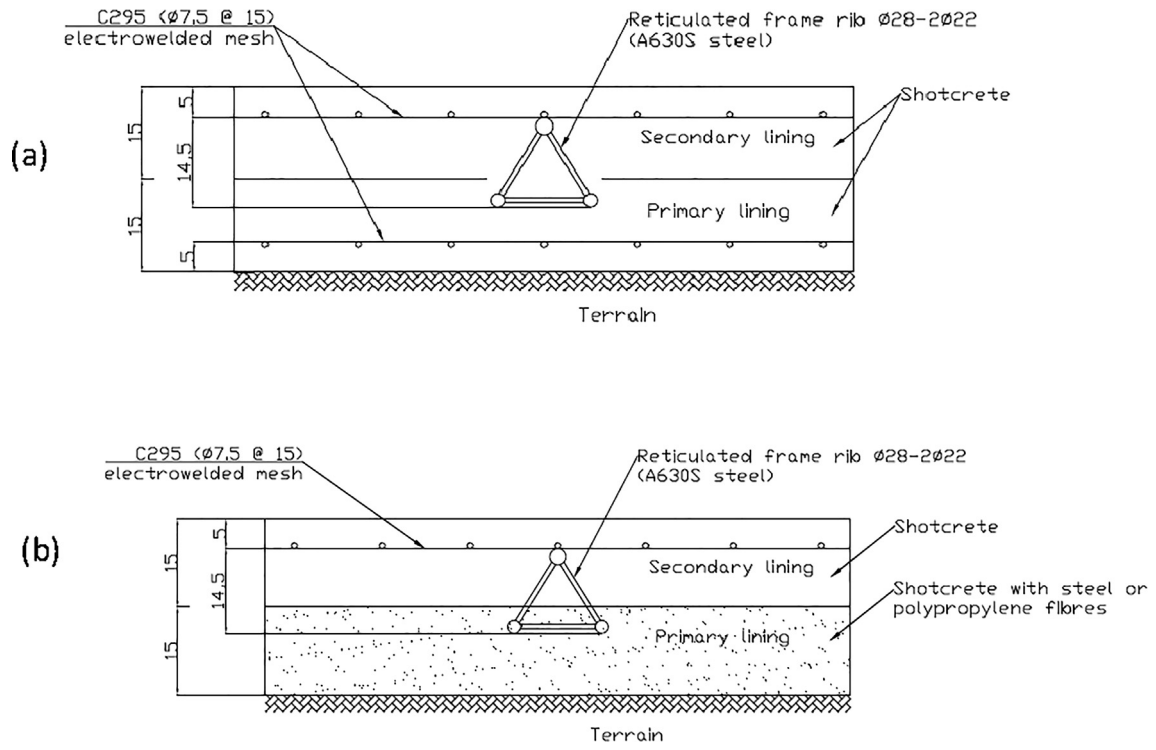

Fig. 1. Sections of the tunnel lining (bottom floor) – (a) Traditional section with double reinforcement of steel welded mesh (primary and secondary lining) and reticulated frame and (b) Proposed section with steel welded mesh in the secondary lining, steel or polypropylene fibers in the primary lining, and reticulated frame.

cycles; (ii) better impact and abrasion behavior; and (iii) increased durability resulting from better cracking control, among others. In addition, in the case of applications where the fibers completely replace the traditional reinforcement, time saving of reinforcement placing can become considerable.

Previous experimental research around FRC (Belletti et al., 2004; Wetzig et al., 2004; Kang et al., 2012) as well as practical usage of FRC in tunnel linings (Chiaia et al., 2009; De la Fuente et al., 2012) can be found mainly in Europe, where the focus has been placed mainly around steel fibers using particular construction methods and technology, as well as shapes and quantity of fibers. On the other hand, polypropylene fibers are currently gaining popularity in the mining industry in Chile and Australia in stiff soil/rock applications, where they are chosen because they are less prone to corrosion and they produce less wear on the machines. Few comparisons can be found in the literature between steel and polypropylene fibers with a particular focus on the structural behavior for shotcrete in tunnels. The motivation of this work is to evaluate the partial replacement of the traditional reinforcement of electrowelded meshes by steel or polypropylene fibers for a subway tunnel in Santiago (Chile), using the fibers and construction technology available and typically used in the Chilean practice. This work carries out an experimental and analytical evaluation of a lining reinforced with electrowelded meshes or with steel or polypropylene fibers. Scaled (1:2) sections under flexo-compression tests are performed on typical sections of shotcrete linings, constructed with concrete with and without fibers, electrowelded meshes, and a reticulated embedded frame. On the other hand, the observed behavior is numerically modeled, and a finite element analysis of the soil-tunnel system is performed to establish the demands to which the tunnel will be subjected, both to static and seismic loads.

2. Design of experiments and construction of specimens

2.1. General description of experiments

The primary objective of the experiments was to evaluate the mechanical behavior of tunnel lining sections structured with reticulated steel frames, shotcrete with fibers (steel or synthetic), and traditional reinforcement meshes subjected to bending, shear and axial loading in the direction perpendicular to the axis of the tunnel. The purpose is to compare the effect of the replacement of the traditional reinforcing mesh with fibers, and to observe the contribution of the reticulated frame.

In order to achieve it, material properties were characterized and also specimens were designed and tested to capture flexural and shear response. With respect to the element tests, 12 bending tests were performed with axial load, with different reinforcement solutions, different half-span to depth ratios (M/Vd, moment-to-shear to reinforcement level arm ratio) and also varying the axial load. The specimens were constructed at 1:2 scale. For the characterization of the material properties, the following additional tests were also performed: (a) bending tests on specimens with indentations and without reinforcement, following the EN 14651 (2007) methodology, (b) compressive tests of cylindrical cores obtained from the test specimens, (c) direct tensile tests on shotcrete cores with and without fibers and (d) uniaxial steel tensile tests of meshes and frames.

According to Nazar (2016), in the actual tunnels under consideration (line 6 of the Santiago Metro), the support (also called the primary lining) is 15 to 25 cm thick, while the lining (also called secondary lining) is of a minimum thickness of 15 cm, being both shotcreted elements. The typical steel meshes used as reinforcement are, depending on the ground type, C295 (295 mm^2/m area) or C338 (338 mm^2/m) grade AT56-50H (f_y = 500 MPa, nominal) electrowelded meshes, with bar diameters of 7.5 mm and 8.5 mm respectively, spaced at 150 mm. In addition, three-bar reticulated frames (one 28 mm diameter bar and two 22 mm diameter bars) of grade A630S steel (f_y = 420 MPa, nominal) or grade A42-27H (f_y = 270 MPa, nominal) with height variable with ground type (145 mm for gravel and 180 mm for soil), and with a variable separation between them, which also depends on the type of ground type (1.0 to 1.5 m for gravel, and 0.5 to 1.0 m for fines or irregular areas) are considered. Fig. 1 shows the sections of the tunnel.

For the purposes of this work, the tunnels found in gravel were

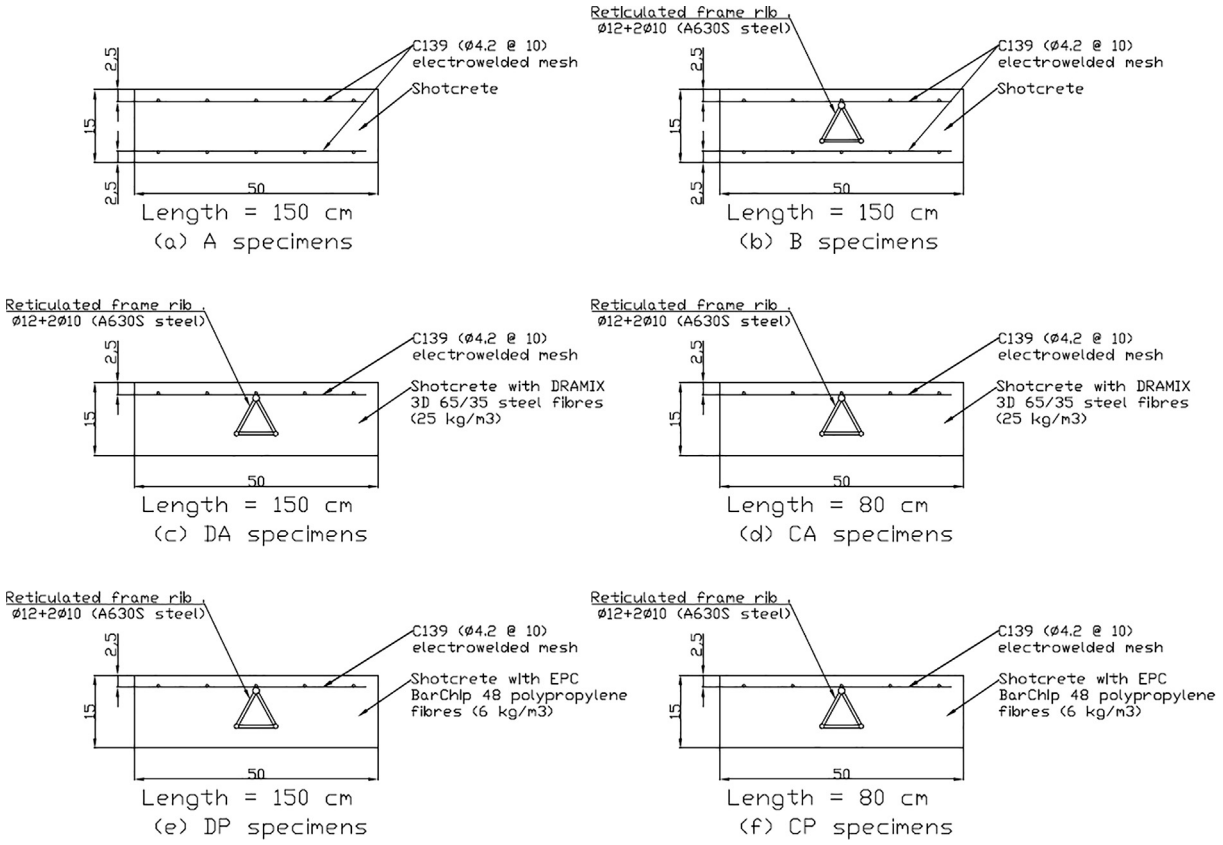

Fig. 2. Characteristics of specimens – (a) A (L = 150 cm), (b) B (L = 150 cm), (c) DA (L = 150 cm), (d) CA (L = 80 cm), (e) DP (L = 150 cm) and (f) CP (L = 80 cm).

Table 1
General characteristics of specimens.

Specimen name	Dimensions			Fibres		Conventional reinforcement		
	Length (cm)	Width (cm)	Height (cm)	Type	Base mix dosage	Upper mesh	Lower mesh	Reticulated frame
A1	150	50	15	None	None	C139 (Φ4.2@100)	C139 (Φ4.2@100)	None
A2								
B1								Φ12 + 2Φ10
B2								
DA1				DRAMIX 3D 65/35 BG	35 kg/m^3		None	
DA2								
DP1				EPC BarChip 48	6 kg/m^3			
DP2								
CA1	80			DRAMIX 3D 65/35 BG	35 kg/m^3			
CA2								
CP1				EPC BarChip 48	6 kg/m^3			
CP2								

Table 2
Concrete mixture description.

Material	Specification	Description	Supplier	Quantity
Cement	Melón Extra	High strength grade	Melón	425 kg/m^3
Sand 1	Melón Semi-Industrial Pozo San Bernardo	Coarse sand	Melón	1303 kg/m^3
Sand 2	Melón José Catalán	Fine sand	Melón	326 kg/m^3
Aditive 1	MX-1390	Water reducing/ plasticising aditive	Sika	2.13 kg/m^3
Aditive 2	Viscocrete 5100	Water reducing/ plasticising aditive	Sika	3.83 kg/m^3
Aditive 3	Microsílice	Microsilica	PSI	29.8 kg/m^3
Water	–	–	–	210 lt/m^3

considered. To maintain the 1:2 scaling, a 15 cm section was considered for the specimen, with a C139 mesh (1.39 cm^2/m) and a frame composed of two 10 mm bars and one 12 mm bar, with a frame height of 80 mm and a separation of 0.5 m. Fig. 2 shows a schematic cross-sections of the specimens along with their longitudinal dimensions. Also, two lengths of the specimens were considered, 1.3 m and 0.5 m as the distance between supports, in order to capture the response of slender and short elements. Table 1 shows the general characteristics of the 12 reinforced specimens.

2.2. Materials and construction of specimens

The test specimens were built within the tunnel to maintain similar process as for the tunnel construction, where the concrete was sprayed with the same characteristics as in the real tunnel construction, except that the concrete was sprayed onto moldings, instead of projecting it

directly onto the ground. Concrete mixtures (see Table 2) were identical for all cases, and fibers were added to the mixture in the plant and then the mixture was transported using a concrete mixer truck to the site to be sprayed. The concrete had a nominal cylindrical strength of 35 MPa, and the actual strength was determined via testing on cored cylinders. The equipment used to spray the concrete was the same used by the contractors to build the actual tunnel, and consisted in (i) a Putzmeister Tk40 pump, with 10 S per minute, (ii) an Atlascopco Xas 420 compressor at 7 bar pressure, and (iii) Sigunit STM-AF Mining setting accelerator in a quantity of 5% of the weight.

Additionally to the specimens described in Table 1, six beam tests were built to characterize the fracture mechanics of the material under bending loading. The beams are 70 cm long, 15 cm wide and high, and a notch of 25 mm (height) was placed in the middle on the tensile side, as dictated by EN 14651 (2007). Steel and polypropylene fibers were used in the same quantities as for the steel reinforced beams tests. In addition, 3 forms of dimensions 500 mm by 500 mm by 300 mm were projected with concrete to extract 10 cm diameter by 20 cm high cylinders.

Dramix 3D 65/35 BG steel fibers were used in a dosage of 35 kg/m^3 and EPC BarChip 48 polypropylene fibers in a dosage of 6 kg/m^3. It is important to mention that in local practice, due to equipment selection, it is considered that these dosages are the maximum dosages that can be specified without generating major construction problems (i.e., pump clogging). Dramix 3D 65/35 BG fibers are non-textured cold-drawn steel fibers of circular cross-section, with single-ended hooks with 0.55 mm in diameter and 35 mm in length (aspect ratio 35/0.55 ~ 65) . The nominal tensile strength is 1345 MPa, with a nominal elastic modulus of 200 GPa. On the other hand, BarChip 48 EPC fibers are longitudinally straight polypropylene (olefins) fibers, 48 mm long with a rectangular section and textured surface. The nominal tensile strength is 640 MPa and the nominal elastic modulus is 12 GPa. Photographs of the fibers are shown in Fig. 3.

2.3. Test setup

The beams are sustained on simply-supported end joints (separated at 1.3 m or 0.5 m) and loaded transversally with an actuator in the center of the beam. All 12 specimens simulate sections of tunnels and therefore have an axial (compressive) load applied that represent the actions over the lining due to ground thrust and the geometric shape of the element. The axial load system consists of two hollow jacks with passing bars of 15 mm in diameter, which are connected to the specimen and jacks end by means of bolted plates. The jacks are placed horizontally and react against a steel beam, which is hold horizontally with the specimens. On the other side of each specimen an equal steel profile is placed with a plate, passing the bar through the steel profile parallel to the specimen and anchored.

To measure displacements of the specimens 5 LVDT were used, with 2 or 3 of them located in the central axis where the transverse load is applied. A load cell was used to measure transverse loading during the test, as well as, a tubular load cell (washer type) was used for axial loading. DSLR cameras were used to measure displacements and deformations through photogrammetry (image correlation). In order to perform the digital image correlation analysis (DIC), the program Ncorr (Blaber et al., 2015) has been used in conjunction with Ncorr_post (Nežerka et al., 2016). Ncorr is an open source program that performs digital image correlation analysis (DIC) and has implemented nonlinear methods of optimization, interpolation using biquintic splines, and is capable of performing analysis at large deformations.

A schematic drawing of the test of one of the slender specimens is shown in Fig. 4. The test of short specimens has a similar testing scheme.

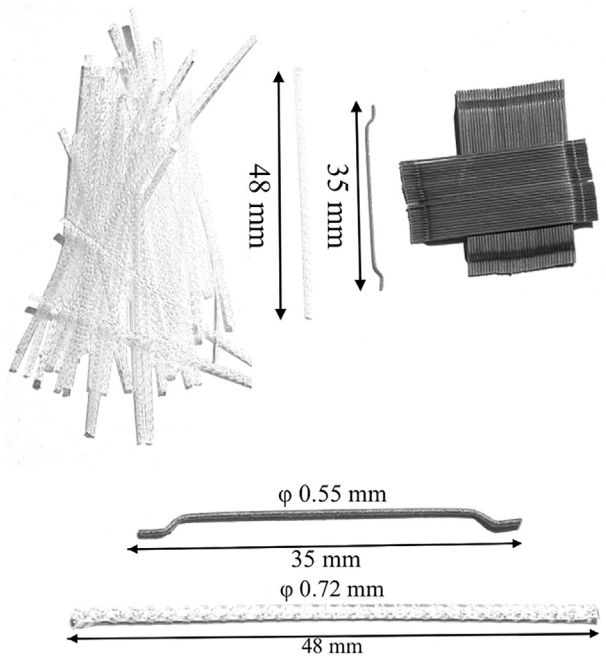

Fig. 3. Fiber comparison for the experimental study (Dramix 3D 65/35 BG and EPC BarChip 48).

3. Experimental results

This chapter details the experimental results, both in terms of overall response and photogrammetry. All tests were performed between approximately 200 and 240 days of concrete maturity, and material properties were characterized at the time of testing.

3.1. Tensile response of steel

Uniaxial tensile tests were performed on the reinforcing steels used for the construction of the specimens. Fig. 5 shows the tensile curves of ϕ10 and ϕ12 bars of grade A630S steel, and of bars ϕ4.2 of grade AT50-56H steel. The solid lines correspond to representative curves of each set of tests. The average yield stress of grade A630S steel was 524 MPa and 498 MPa (diameters of 10 mm and 12 mm, respectively), whereas for grade AT50-56H steel it was 557 MPa. As shown in Fig. 5, the steel grade AT56-50H achieves a fracture strain of just about 1.5%, whereas the steel grade A630S, on the other hand, reaches a fracture strain of 7% or more.

3.2. Shotcrete in compression

Uniaxial compression tests were performed on cylinders (3 per type) of shotcrete with and without fibers, with dimensions of 100 mm in diameter and 200 mm in height. The specimens where cored as per ASTM C42/C42M. The average capacity of plain concrete was 55.3 MPa, whereas for the concrete with steel fibers it was 59.9 MPa. In the case of concrete with polypropylene fiber, one of the specimens had an anomaly and was discarded, resulting in an average of 55.7 MPa. The stress-strain relationships obtained from the experiments are shown in Fig. 6. It is possible to appreciate that the addition of steel fibers gives a slightly greater ductility to the material, switching the deformation at peak strength from 0.25% to 0.4%. For the case of polypropylene fibers, the results were less conclusive.

3.3. Shotcrete in tension

Direct tension tests were carried out on 100 mm diameter and 200 mm high shotcrete (with and without fibers) specimens with a 10 mm center notch running around the perimeter (implying an

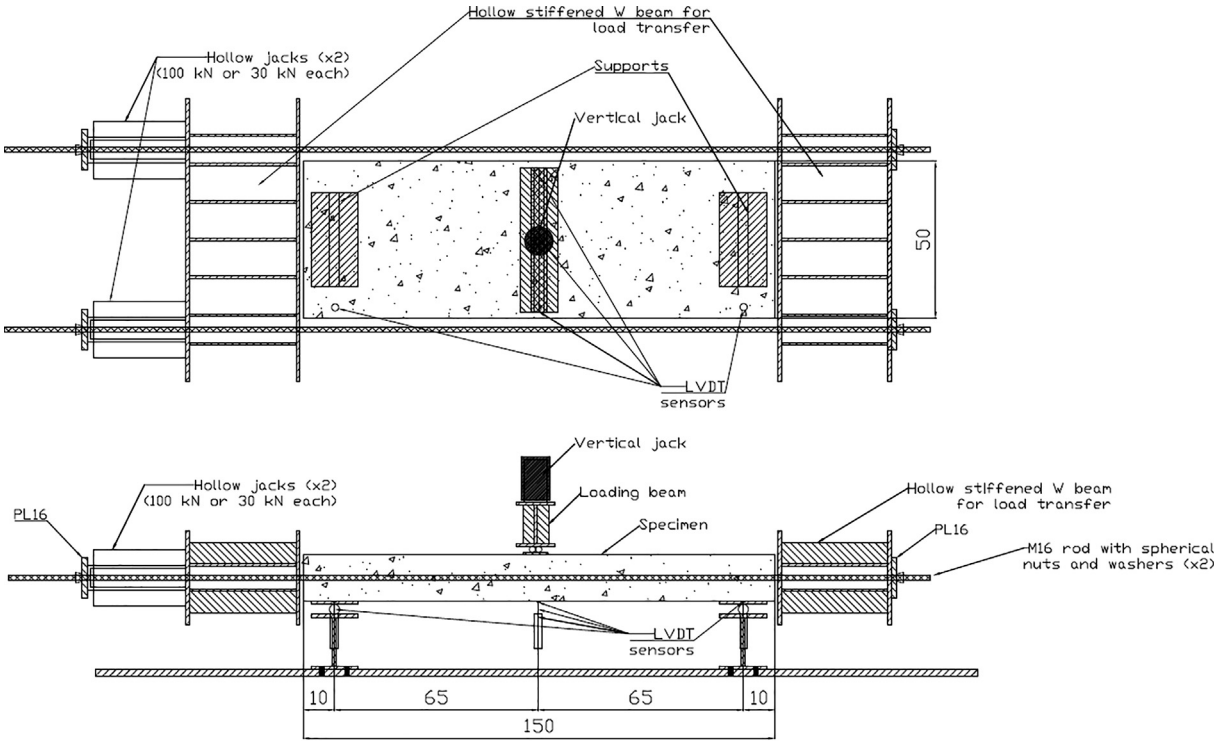

Fig. 4. Test scheme for a beam with axial load (slender beams).

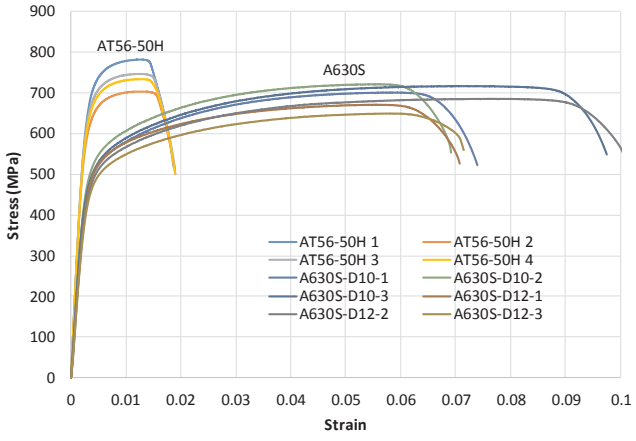

Fig. 5. Tensile steel tests for types A630S and AT56-50H.

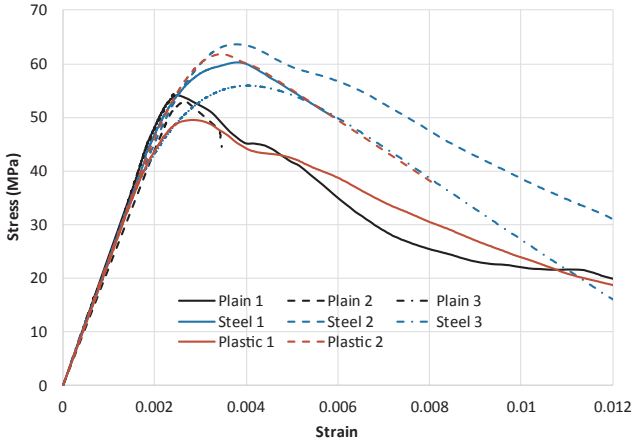

Fig. 6. Stress versus strain response of concrete cylinders in compression.

effective diameter of 80 mm in the central area, that is, an effective area reduced by 36%). The specimens are cored as per ASTM C42/C42M. Each specimen is glued (epoxy) between plates, and these plates are attached to universal testing machine clamps, that pull the core in tension. Two specimens were tested per type, and in 4 of them (both specimens with steel fibers, one with polypropylene fibers and one without fibers) failure occurred outside the notch (see Fig. 7a), indicating that the material is not homogeneous and has a capacity at least 36% lower in the wider section. The tensile strength based on the reduced section was very variable, with values ranging between 1.5 MPa and 2.5 MPa for plain concrete, 1.1 MPa and 1.6 MPa for concrete with polypropylene fiber, and 0.3 MPa and 0.5 MPa for concrete with steel fibers. When inspecting the specimens, it was observed that very few fibers crossed the crack, with most of the fibers having an orientation parallel to the crack probably due to the direction of concrete projection (perpendicular to the extraction). The higher capacity of the unreinforced specimens suggests that the fibers generated a failure plane reducing their capacity.

3.4. Bending tests on prisms

Two specimens per fiber type for bending tests were carried out under controlled procedure EN 14651 (2007) on shotcreted prisms (over molds) of dimensions 150 mm in height, 150 mm in width and 700 mm in length; with spacing between supports of 500 mm. Testing of the test specimens without fibers was not performed. Unlike the direct tensile test (in this case the fibers would be sprayed placing them parallel to the loading direction), all test specimens have similar capacities and consistent with the expected strength for the plain concrete. The impact on fiber ductility is appreciable where steel works from the first cracking stage, whereas polypropylene requires a larger crack size (vertical displacement) to observe its effectiveness. Fig. 8 shows the results.

Fig. 7. Tensile test of concrete cylinders – (a) failure in the unreduced section, and (b) failure in reduced section.

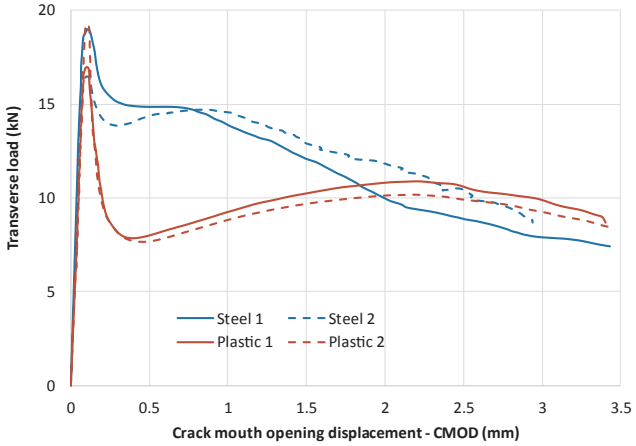

Fig. 8. Load versus deflection response of prism.

3.5. Bending tests of beams with axial load

Twelve flexural tests were performed (Figs. 9–14), with different bearing lengths (to observe the shear stress impact), as well as reinforcement configuration and axial loads. The axial loads were chosen (60 kN and 200 kN) to be consistent with the tunnel under study, and such variable was relevant considering that the axial load can have an important impact on ductility (Wallace et al., 2008). Table 3 shows the specimen description.

All settlement or adjustment of supports observed in the specimens, especially the ones with large transversal strength (short beams), was corrected in the central LVDTs by subtracting the support settlements. Another important aspect to note is that initially specimens CP2 and CA2 used spacing between supports of 500 mm, however, as a shear (diagonal) failure was not observed, the separation was changed to 400 mm for the specimens CP1 and CA1.

3.5.1. Specimens A1 and A2

Specimens A1 and A2 have a single central bending crack (without the presence of minor cracks) starting at approximately 20 kN and 27 kN, respectively (Fig. 9). Both reach similar capacities (40 kN). In the case of A1, there is a rapid degradation that ends with fracture of the bottom steel mesh. In the case of A2, the test was stopped before reaching the fracture of the upper steel mesh (the bottom steel mesh was fractured). Specimen A2 (higher axial load) offers much more ductility than A1 (lower axial load), but has very similar load carrying capacity (Fig. 15).

3.5.2. Specimens B1 and B2

Specimens B1 and B2 have a slightly higher cracking load than the ones without the reticulated frame (A1 and A2), with loads of 24 kN and 30 kN, respectively. In this case, however, the damage progresses concentrated in a central flexural crack, but there are minor secondary flexural cracks (Fig. 10). Again, it is appreciated that the effect of the larger axial load is almost negligible in terms of capacity. This time the ductility is higher for the low axial load case, which is explained by the presence of the reticulated frame, which gives more ductility in both specimens, with great impact compared to the specimens without the frame (Fig. 15). In both specimens (B1 and B2) the bottom steel mesh was found fractured at the end of the test. The reticulated frame did not fracture.

3.5.3. Specimens Da1 and Da2

Specimens DA1 and DA2 presented similar behavior to specimens B1 and B2, with a central bending crack (this time somewhat diagonal – Fig. 11) and minor secondary bending cracks, although in the case of DA2 there are practically 2 main cracks (Fig. 11b). These cracks start approximately at loads of 21 kN and 24 kN, respectively. The maximum loads are similar in both specimens. At the end of the test it is possible to verify that the steel fibers close to the tensile side failed due to sliding. No fracture is observed in the steel mesh or frame. Again, it is appreciated that the effect of the larger axial load is almost negligible (Fig. 15).

Fig. 9. Failure mode – (a) specimen A1 and (b) specimen A2.

Fig. 10. Failure mode of specimens B1 and B2 – (a) concrete cracking and (b) fracture of inferior steel welded mesh.

3.5.4. Specimens Dp1 and Dp2

Specimens DP1 and DP2 presented similar behavior to specimens DA1 and DA2, showing 2 main central bending cracks (somewhat diagonal) and minor secondary flexural cracks (Fig. 12). These cracks start approximately at loads of 18 kN and 32 kN, respectively. The maximum loads are similar in both specimens. At the end of the test, only the bottom steel mesh was fractured. It is possible to verify that the polypropylene fibers close to the tensile side rupture. Fig. 12b shows the damage concentration in the center, but this time distributed over a larger length than the previous tests.

3.5.5. Specimens CA1 and CA2

The axial load remained constant, however, in the CA1 experiment, the stroke of the axial actuators did not reach to accommodate the change of length during the experiment, increasing the axial load to 110 kN at the end of the test (at an central displacement of 12.0 mm). Specimen CA1 presented cracking at an estimated load of 85 kN, while CA2 at a load of 70 kN. The damage progresses concentrated in a central crack in the case of CA2 and in two main central cracks for CA1 (bending and diagonal tension), without secondary cracks (Fig. 13). Post-peak degradation is less pronounced than in the case of slender specimens (Fig. 16).

3.5.6. Specimens CP1 and CP2

Specimens CP1 and CP2 presented a behavior similar to CA1 and CA2. Specimen CP1 showed cracking at an estimated load of 75 kN, while CP2 at a load of 90 kN. The damage progresses concentrated in a central crack (bending and diagonal tension), without secondary cracks (Fig. 14). Post-peak degradation is less pronounced than in the case of slender specimens (Fig. 16).

3.5.7. Load-displacement responses

The overall load versus displacement (central) response is shown for all cases in Figs. 15 and 16. In general terms, for the slender specimens (Fig. 15), it can be seen that the reticulated frame has a very important influence on both the specimen strength and ductility, which can be seen by comparing the response of specimens A (without frame) with specimens with frame, both with steel mesh (B) and with fibers (DA and DP). It is also possible to conclude that the fibers contribute to sectional capacity as much as or even more than the welded steel mesh, although this contribution is modest. It is observed that the specimens with steel fibers have a behavior similar to that of the B specimens (frame and double mesh), while the specimens with polypropylene (DP) fibers have sectional capacities somewhat larger than the specimens comparable with frame (DA and B), showing at the same time minor ductility. The higher axial load results in faster strength degradation for all specimens. In the case of short specimens (Fig. 16), higher capacity and lower ductility is observed in all specimens, compared to slender specimens. Small differences are observed between both fiber types, with slightly earlier initiation of degradation of specimens with polypropylene fiber. The impact of axial load is less evident than with slender specimens.

For damage distribution purposes, photogrammetry was used by measuring the tensile strains at the most tensioned edge to estimate curvatures and a plastic hinge length (Dias-da Costa et al., 2014). For that, the integral of the strain (ε) distribution at a particular beam deflection δ (considering the small compressed zone or the almost constant neutral axis depth in the beam length, this value is consistent with the curvature distribution) normalized by the maximum tensile strain (ε_{max}) obtained by photogrammetry, was defined as plastic hinge length ($l_p = \int \varepsilon dx/\varepsilon_{max}$). This value is again normalized by the beam height (l_p/H_f) for convenience and familiarity. The results, summarized in Table 4, indicate that the damage in slender specimens is much more concentrated on specimens without reticulated frame, and within the framed specimens, polypropylene (DP) specimens distribute damage (i.e., have a higher plastic hinge length l_p) much more than the other (comparable) solutions.

4. Analytical studies

This chapter presents an analytical study focused on quantifying forces and demands on the lining of the tunnel under study.

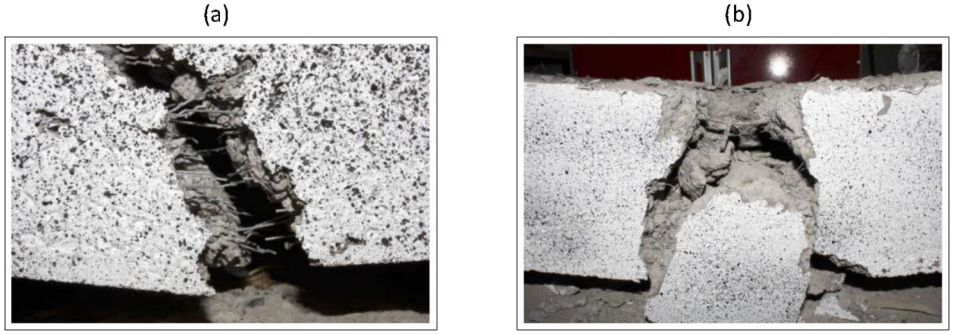

Fig. 11. Failure mode of specimens DA1 and DA2 – (a) Fiber adherence failure, and (b) cracking in specimen DA2.

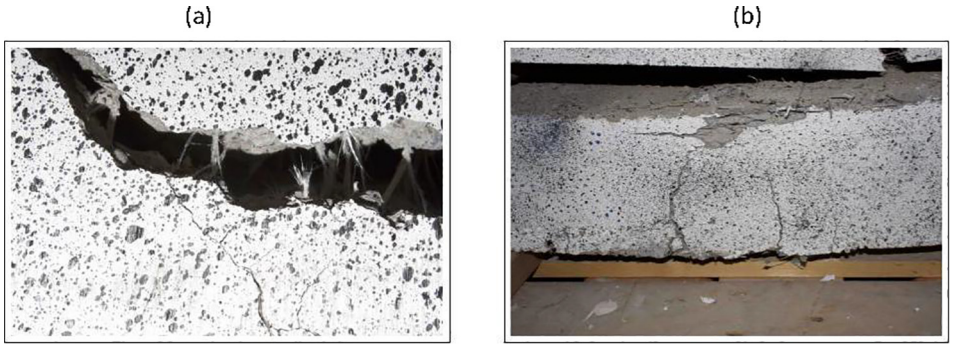

Fig. 12. Failure mode of specimens DP1 and DP2 – (a) tensile rupture of the polypropylene fibers, and (b) cracking of specimen DP1.

4.1. Experimental test models

All specimens were modeled in OpenSees (Mazzoni et al., 2006), an Open Source object-oriented platform developed at UC Berkeley to simulate the response of structural and geotechnical systems, with an extensive library of research-focused elements and material models. The models used in this study are based on a fiber section (bending-axial) model composed by steel and concrete longitudinal fibers (cross-section is discretized accounting for concrete and steel components). For steel, the uniaxial model by Chang and Mander (1994) was selected (Fig. 17c), whereas, for concrete in compression the model by Chang and Mander (1994) was also considered (Fig. 17a). A fiber model (Taucer et al., 1991) of the EN14651 test was performed using distributed plasticity elements (nonlinear behavior of steel and concrete fibers are incorporated in longitudinal elements with 3 degrees per node – 2D case – that follow the Bernoulli hypothesis) to determine the appropriate parameters for modeling the tensile response of concrete (Fig. 17b).

Also, the scaled bending tests (beams with axial load) were modeled with fiber sections based on the constitutive laws derived for material characterization tests. Figs. 15 and 16 show the experimental results compared with the numerical simulations. As it can be seen, the models are able to simulate the general response (stiffness, strength, degradation, failure of the reinforcement) reasonably well. Considering that tunnel tolerances are not tight and that the actual thickness varies greatly due to the nature of the work, the modelled behavior is good enough to capture the general flexural response of the section (capacity, stiffness, failure of the rebar, etc.) with sufficient accuracy for the purpose of modelling the tunnel lining for all specimens.

4.2. Tunnel finite element model

The finite element model of the tunnel consists of a two-dimensional model of the cross-section of the tunnel-soil system, which will be subjected to an ovalling analysis, that is, a pseudo-static desangulation, such that with a simple model of the transversal seismic response of the tunnel-soil system one can establish the demands on the lining of the tunnel.

The soil is modeled with bi-quadratic quadrilateral elements of 9 nodes and a nonlinear material model PDMY02 (Yang and Elgamal, 2000). The lining is modeled with beam-column elements of fiber sections with non-linear uniaxial material models, calibrating the steels and concrete properties from previous analysis that are validated with the scaled bending experiments as well as the uniaxial tests. Finally, the soil-structure interaction was modeled with rigid springs in compression and with zero stress in tension for the perpendicular direction, and in the tangential direction with a concrete-soil friction model of perfect adhesion. The nonlinearity associated with the materials (soil, concrete and steels) has been modeled, but not geometric nonlinearity. The final model has approximately 8200 quadrilateral elements (32,000 nodes), 250 beam-column elements (800 nodes) and 250 contact elements (800 nodes). The mesh chosen to perform all analyses (Fig. 18) has good discretization for the number of nodes, not excessive elements and follows general guidelines from state of the art meshing techniques (Beer, 2012; Potts, 2002), with special attention to element regularity and avoidance of boundary effects (such as a large domain and appropriate boundary conditions).

4.2.1. Elements and materials

For the gravel considered as part of the soil-structure model, PDMY02, a multi-yield material having a failure surface of the Drucker-Prager type (Yang and Elgamal, 2000) with a hyperbolic stress-strain relationship is used, which is capable of stress redistribution. For purposes of calibration the parameters of the monotonic response (compression), values are fitted with model simulations of triaxle tests from the literature for the soil under consideration (De la Hoz Alvarez, 2007; Kort et al., 1979). These values are shown in Table 5, and correspond to a 52° internal friction angle, a depth dependent (Z) elastic modulus from Kort et al. (1979), and a Poisson coefficient of 0.25. The lining was modeled with non-linear fiber-based beam-column elements (material and geometrical nonlinearity, although the latter has little impact). The use of these elements, which do not model the shear response, can be justified noting that at the area under interest (vault area), the slenderness of lining is controlled by flexural response, and according to the experimental tests on beams, for the geometry and levels of axial load considered, the model captures the overall response (Figs. 15 and 16).

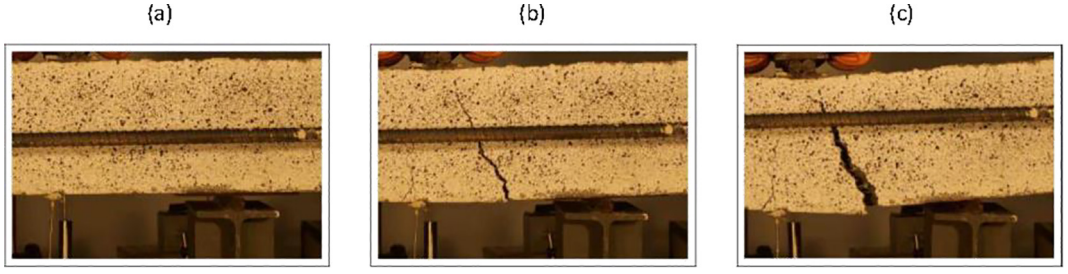

Fig. 13. Growing of the principal crack of specimen CA1 – (a) δ = 5.9 mm, (b) δ = 12.1 mm and (c) δ = 15.1 mm.

Fig. 14. Specimens CP1 and CP2 – (a) CP1 at δ = 13.1 mm and (b) CP2 at δ = 9.9 mm.

Table 3
Reinforcement and loading condition of specimens.

Specimen	Reticulated frame?	Tensile reinforcement	Support distance (m)	N (kN)	N/Agf'c (%)
A1	No	Φ4.2 @ 100 mesh	1.3	60	2%
A2	No	Φ4.2 @ 100 mesh	1.3	200	7%
B1	Yes	Φ4.2 @ 100 mesh	1.3	60	2%
B2	Yes	Φ4.2 @ 100 mesh	1.3	200	7%
DA1	Yes	Steel fibres	1.3	60	2%
DA2	Yes	Steel fibres	1.3	200	7%
DP1	Yes	Polypropylene fibres	1.3	60	2%
DP2	Yes	Polypropylene fibres	1.3	200	7%
CA1	Yes	Steel fibres	0.4	60	2%
CA2	Yes	Steel fibres	0.5	200	7%
CP1	Yes	Polypropylene fibres	0.4	60	2%
CP2	Yes	Polypropylene fibres	0.5	200	7%

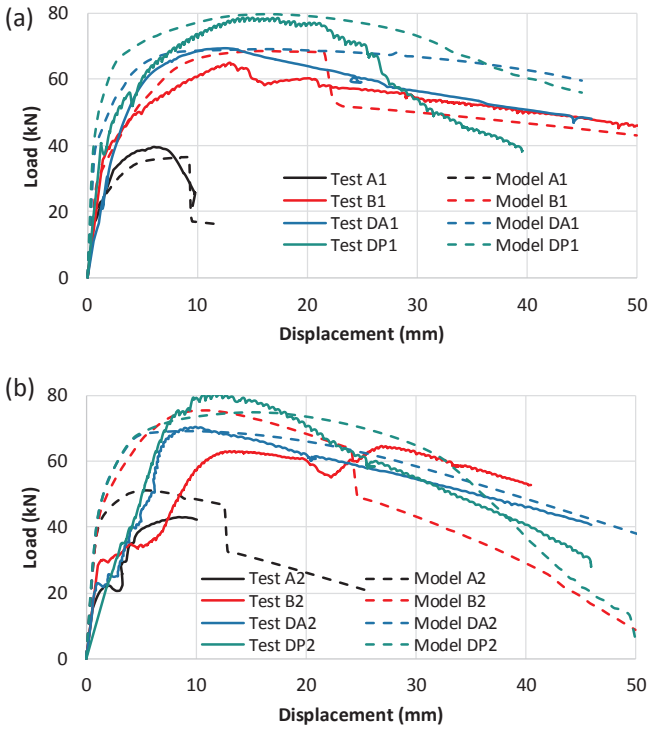

Fig. 15. Transversal load versus transversal displacement test and model response for slender specimens – (a) specimens with low axial load and (b) specimens with high axial load.

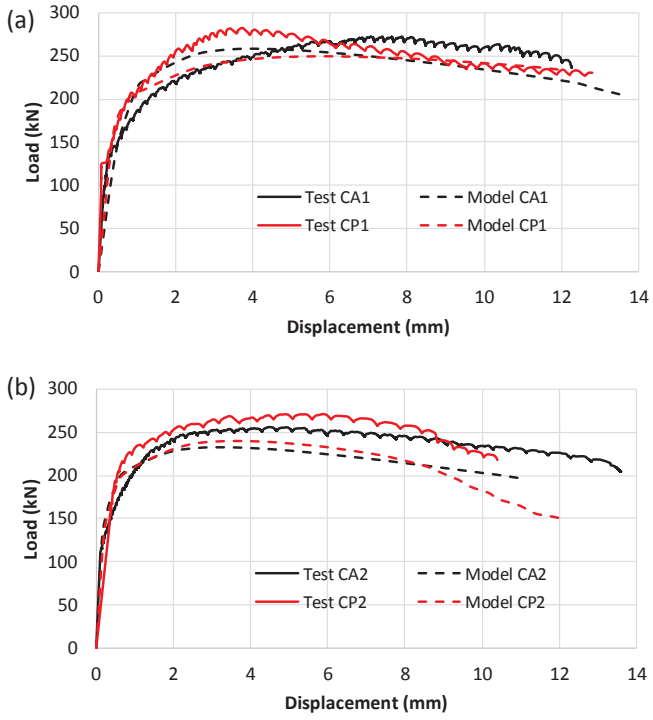

Fig. 16. Transversal load versus transversal displacement test and model response for short specimens – (a) specimens with low axial load and (b) specimens with high axial load.

Table 4
Measured plastic hinge length.

Specimen	Estimated lp (mm)	lp/Hf	Measured δ (mm)
A1	125	0.83	10
A2	128	0.85	38
B1	171	1.14	54
B2	195	1.3	42
DA1	164	1.09	44
DA2	161	1.07	47
DP1	263	1.75	43
DP2	247	1.64	50
CA1	154	1.02	15
CA2	129	0.86	14
CP1	113	0.75	14
CP2	162	1.08	14

In order to impose an oval deformation on the system, auxiliary elements were used that are not part of the conceptual model, but allow a simpler analysis. Rigid bars were placed on the side edges of the floor grid, connected between them and the adjacent floor by horizontal (non-vertical) rigid springs, allowing the bars to rotate around their

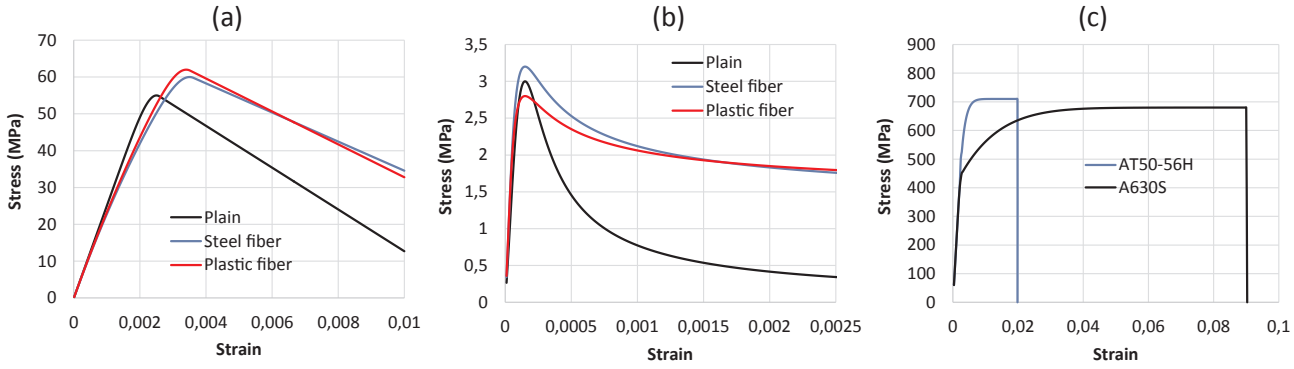

Fig. 17. Material constitutive laws – (a) concrete in compression, (b) concrete in tension, and (c) steel.

respective supports (Fig. 19). Considering that in the analysis a shear deformation (desangulation) will be imposed on the model, the lateral displacement of degrees of freedom of the left and right elements are constraint (connected) at the top and along the edge. For the definition of the cross-section, the scheme of Fig. 1a will be used (since small differences were observed for fibers with the presence of the reticulated frame). Because the section is constructed in a sequential manner (the support is first placed with the reticulated frame, and then the lining), the tension state of the section should be estimated considering this aspect, assuming that the support is loaded first, then the lining connected, and finally the entire section is loaded.

Table 5
Soil-tunnel model parameters.

Parameter	Value	Source
E, Elastic modulus	E = 46 000 (Z (m))^(0.55) (kPa) if Z < 6 m E = 54 000 (Z (m))^(0.53) (kPa) if Z > 6 m E > 100 000 (kPa)	From Kort et al. (1979)
Poisson's Ratio	0.25	From Kort et al. (1979)
Internal friction angle	52°	From Kort et al. (1979) and simulations

4.2.2. Loads and model sequence

On a tunnel in the ground there are essentially two loads of interest in the design: (i) the thrust of the soil resulting from gravity; and (ii) the thrust of the soil caused by an earthquake. The stresses generated by loads acting on the soil surface are typically negligible for most cases.

The modeled load sequence considers a series of stages: (1) application of gravity to the soil not affected by the excavation. These loads are modeled as body forces on each element of soil without excavating; (2) generation of the excavation (opening) in the soil model without support. In the 2D model, this is done by partially flexibilizing the internal material of the excavation by a factor of $\alpha = 0.5$ (Alpha Method – Möller, 2006). This generates redistribution of body forces; (3) placement of the support (primary lining) in the finite element model and new flexibilization of the internal material by a factor of $\alpha = 0.1$, which simulates the advance of the excavation. This new redistribution translates into support loads; (4) placement of the coating (secondary lining) in the finite element model, and a new and final flexibilization of the internal material by a factor of $\alpha = 0.01$, which simulates the possible relaxation over time of the surrounding material. In this way, this new redistribution allows loading of the secondary lining; and finally, (5) application of the seismic model, which in this case is a lateral load as a desangulation to the soil.

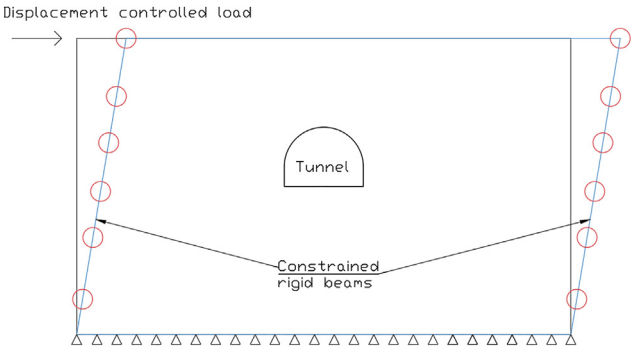

Fig. 19. General tunnel model scheme.

4.2.3. Gravitational and seismic loads (Oval)

In Chile, the value of $\gamma = 0.035\%$ for gravel has been used as desangulation. These values come from the highway design code (Chilean Ministry of Public Works, 2000), which is based on the proposal by

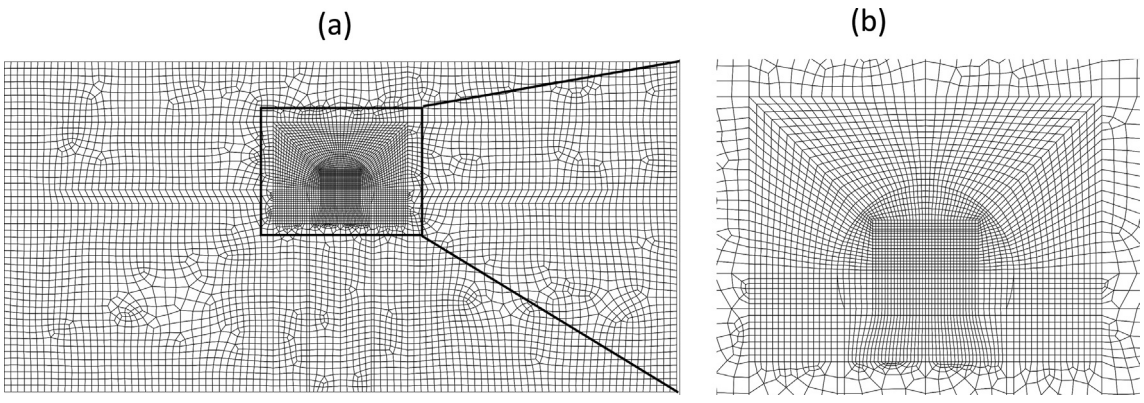

Fig. 18. Soil-tunnel mesh – (a) overall domain and (b) local tunnel diagram.

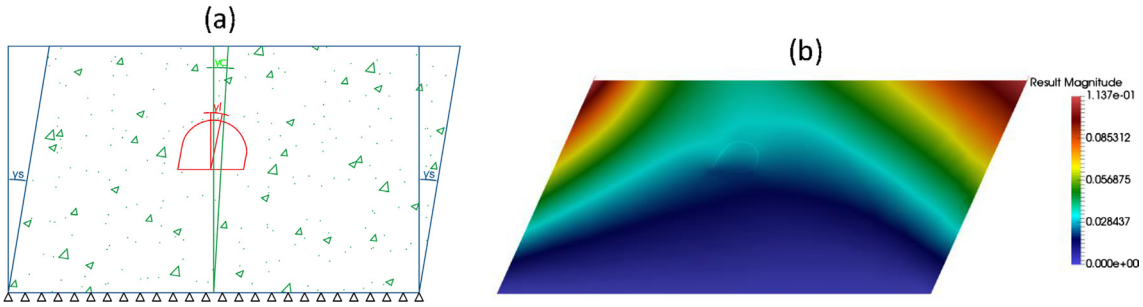

Fig. 20. Desangulation interaction factors – (a) desangulation scheme, and (b) heat map of nodal horizontal displacements.

Kuesel (1969). This proposal assumes, as do most of seismic design methods for underground structures (Hashash et al., 2001), that the design-controlling load is the product of vertical shear waves that travel through the tunnel during the earthquake, and other seismic waves are considered negligible.

It is important to recognize that the model will be deformed on the side frame, such that the desangulation of the ground in the center (tunnel location) is not necessarily the same observed on the side. In addition, due to the kinematic interaction between the tunnel and the lining, the desangulation within the tunnel is not the same as the desangulation of the ground in the same location. Consequently, there are three desangulation magnitudes in the model: (i) γs, desangulation of the ground (soil) on the side; (ii) γc, desangulation of the soil at the center (tunnel location); and (iii) γl, desangulation of the lining. The description of the desangulation magnitudes is shown in Fig. 20a. A heat map with the actual kinematics of the complete system is shown in Fig. 20b for a value of $\gamma c = 0.035\%$. The relationship results obtained for the pushover analysis between these desangulation magnitudes is shown in Fig. 21. Thus, the interaction factor R for $\gamma c = 0.035\%$ is 1.76 (Fig. 21b), implying that the desangulation in the lining would be $\gamma l = 0.062\%$.

Following the positive moment and forces convetion shown in Fig. 22, Fig. 23 shows the internal forces and moments obtained in the support and lining for different desangulation values (γl). After examining the sectional strains and forces it can be seen that both the primary and secondary lining remain in the linear range and therefore the curvature values are obtained linearly from moment-curvature relationship (M-ϕ). There is a concentration of moments (and curvature) in the lower corner of the tunnel, which is not shown since the analysis is focused on the support and lining that cover the upper section of the tunnel (dome). The increased section and geometry of the lower section of the tunnel should be studied and modeled locally. This is consistent with experience in rectangular tunnels, where corners are typically designed for yielding, while the rest of the structure remains linear.

Fig. 24 shows the sum of the loads between the lining and the support. Accordingly, and recalling Fig. 23, the demands on the support and the lining are practically the same. The above shows the preloading

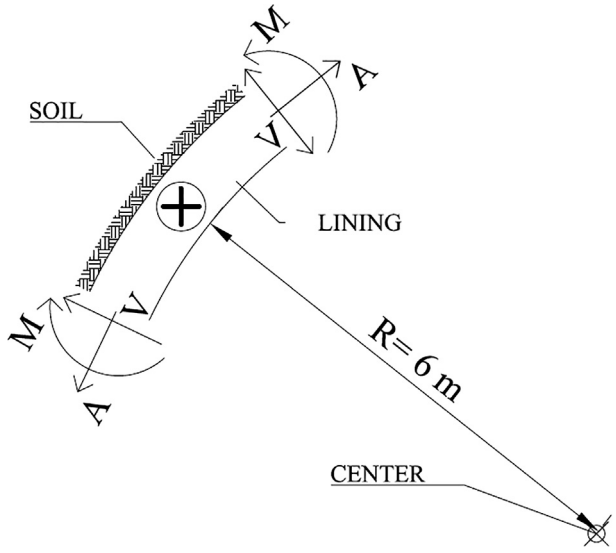

Fig. 22. Convention for positive internal forces and moments.

of the first lining (support) has no significant final effect on the complete capacity of the section, because the preload compressive stresses are low. It is also worth mentioning that even using lower values for α the conclusion is maintained, because the surrounding soil is very stiff and the disequilibrium produced by the excavation is taken by the soil arch effect rather than the lining effect.

Fig. 25 shows the interaction diagram M-N that reveals the moment versus axial capacity for the entire section, with and without the frame contribution. The solicitation is obtained from Fig. 24, for a $\gamma l = 0.09\%$ desangulation, which could be interpreted as an upper limit for the local design. In terms of capacity, the safety factors associated with loads results in very conservative design, independent of the axial load, when the reticulated frame is considered as structural component.

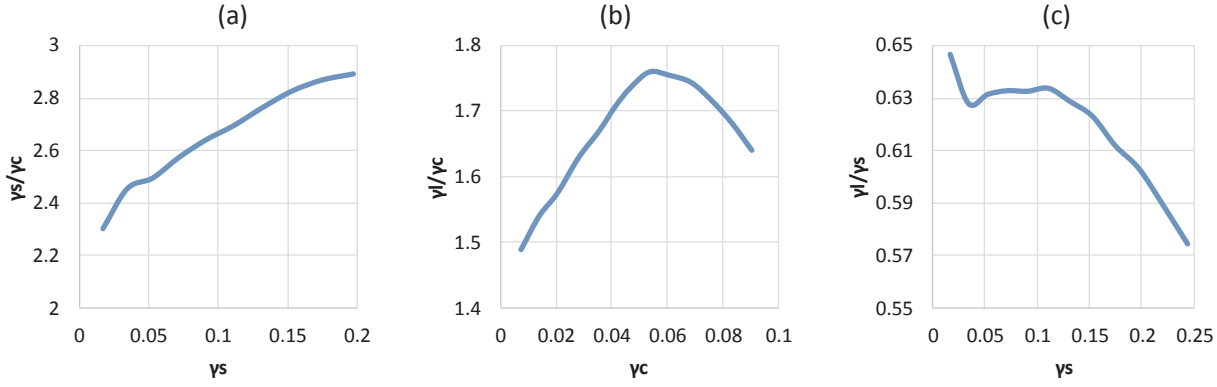

Fig. 21. Desangulation interaction factors – (a) $\gamma s/\gamma c$, (b) $\gamma l/\gamma c$, (c) $\gamma l/\gamma s$.

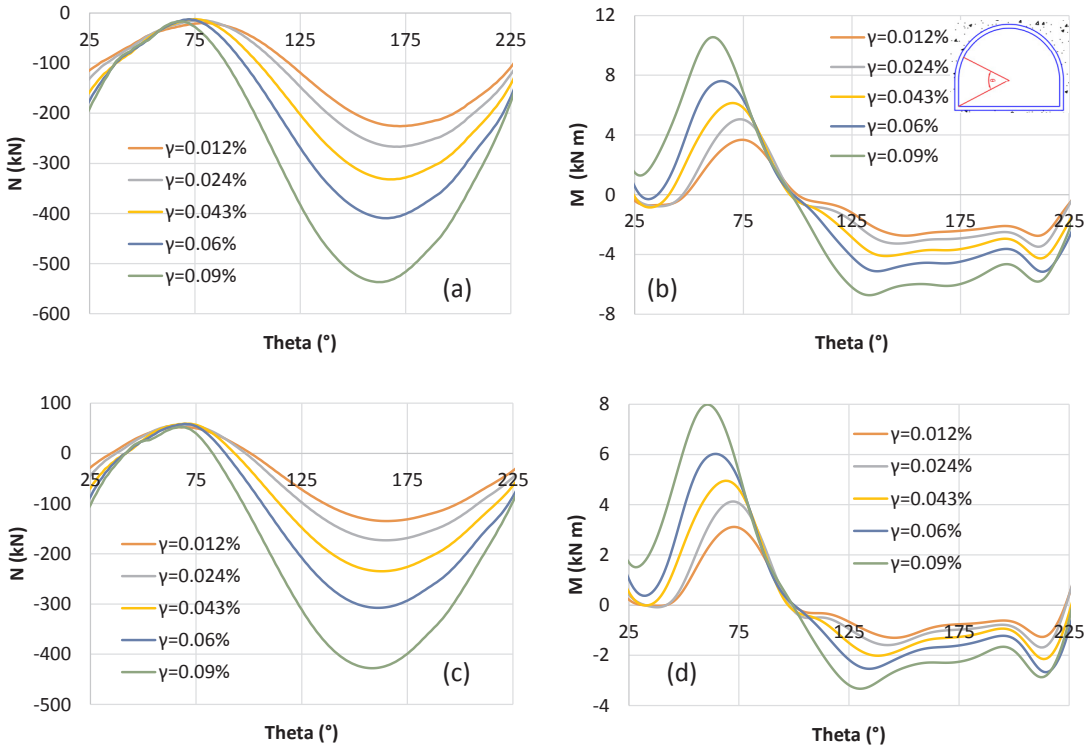

Fig. 23. Dome forces – (a) axial force in the support, (b) moment in the support, (c) axial force in the lining, and (d) moment in the lining.

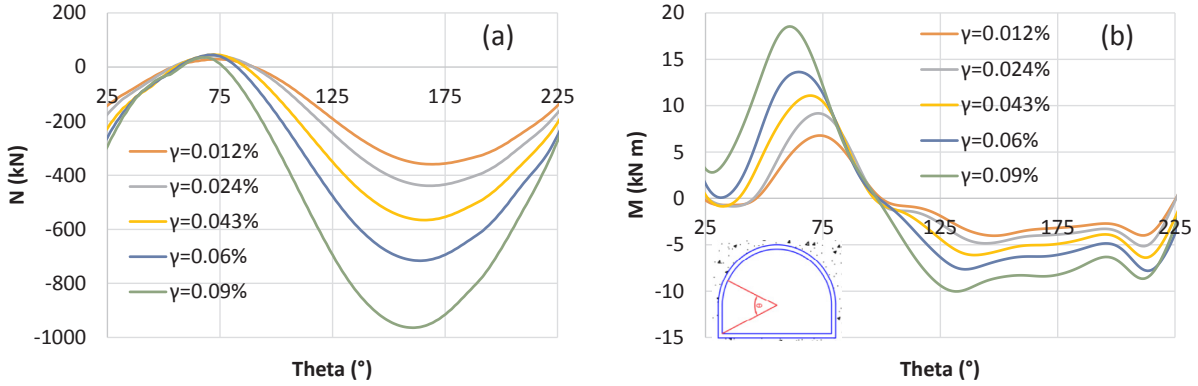

Fig. 24. Dome forces in the entire section – (a) axial force, and (b) moment.

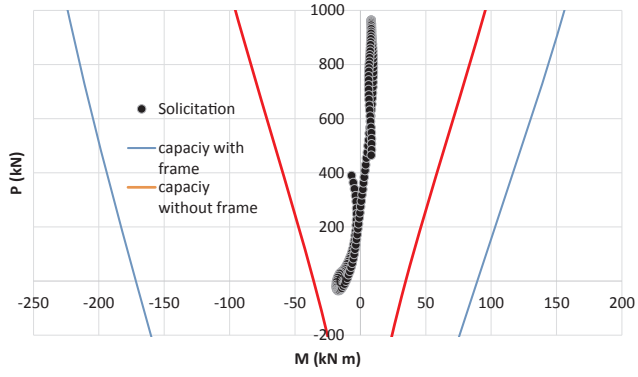

Fig. 25. P_n-M_n interaction diagram.

When the frame is not considered, the capacity is largely reduced, resulting in less conservatism, especially when the axial load is modest, that is, for shallow tunnels.

5. Conclusions

In this study, the use of steel and polypropylene fibers as replacement of welded mesh reinforcement for lining in tunnels has been investigated. A series of tests to characterize the material, as well, as beam tests with axial load are carried out to mimic the gravitational and seismic actions in the lining of the tunnel. Additionally, analytical models are constructed that reproduce the test results and are used to model the tunnel lining in a 2D finite element model of a ground-tunnel model to predict the seismic response under a desangulation given by vertical shear waves.

The concrete tensile characterization using test of prims under bending allows to adequately predicting the response of beams. However, the direct tensile tests of concrete cylinders with and without fibers show a high scatter, resulting in especially low strength values for the cases with fiber, with the case of steel fiber showing the lowest value. It is observed that there is a failure plane where the fibers are oriented parallel to the section, which reduces their capacity.

Regarding the beam with axial load response, it has been found that

replacement of the steel mesh by steel fibers, under the conditions of the tests carried out, and including the reticulated frame, delivers sectional capacities approximately equal to the solution with steel mesh, and presents similar ductility indicators. For the case of polypropylene fibers, for slender specimens, the solution presents sectional capacities approximately 20% higher than the steel mesh solution, with a lower ductility, but a larger distribution of damage. Also, it was found that the reticulated steel frame presents the most important contribution in flexure, in both strength and ductility. The use of non-ductile steel mesh, which presents fracture around 1.5% strain, results in low deformation capacities in the beam with axial load tests. This is observed in the specimens without reticulated frame. Short beam specimens show little differences for both fiber solutions. The overall response of all beam specimens with axial load was well captured by flexural models.

The tunnel model, with the defined properties based on the carried out tests, indicates that for the solicitations estimated for the soil gravel in Santiago, the response remains in a low range of moment and axial load with a practically linear behavior in the seismic phase.

Acknowledgements

The authors would like to acknowledge the support and aid from the Civil Engineering department at Universidad de Chile, where the testing was done. They would also like to thank Metro de Santiago, and in particular to Mr. Edgardo González, for their cooperation and funding provided to build the specimens.

Appendix A. Supplementary material

Supplementary data associated with this article can be found, in the online version, at https://doi.org/10.1016/j.tust.2018.03.027.

References

Beer, G., 2012. Numerical simulation in tunnelling. Springer Science & Business Media.
Belletti, B., Cerioni, R., Meda, A., Plizzari, G., 2004. Experimental and numerical analyses of FRC slabs on grade. In: Proceedings of FRAMCOS5 Conference, Vail Colorado, pp. 973–980.
Bentur, A., Mindess, S., 2006. Fibre Reinforced Cementitious Composites, second ed. Taylor & Francis, Modern Concrete Technology.
Blaber, J., Adair, B., Antoniou, A., 2015. Ncorr: Open-Source 2D Digital Image Correlation Matlab Software. Exp. Mech. 55 (6), 1105–1122.
Chang, G., Mander, J.B., 1994. Seismic energy based fatigue damage analysis of bridge columns: part 1-evaluation of seismic capacity. Tech. rep. MCEER, University of Buffalo.
Chiaia, B., Fantilli, A.P., Vallini, P., 2009. Combining fiber-reinforced concrete with traditional reinforcement in tunnel linings. Eng. Struct. 31 (7), 1600–1606.
Chilean Ministry of Public Works, 2000. Highway Design Manual.
De la Fuente, A., Pujadas, P., Blanco, A., Aguado, A., 2012. Experiences in Barcelona with the use of fibres in segmental linings. Tunnell. Underground Space Technol. 27 (1), 60–71.
De la Hoz Alvarez, K., 2007. Estimation of shear resistance parameters in coarse granular soils (in Spanish). Master thesis, University of Chile.
Dias-da Costa, D., Valença, J., do Carmo, R., 2014. Curvature assessment of reinforced concrete beams using photogrammetric techniques. Mater. Struct. 47 (10), 1745–1760.
EN-14651, 2007. Test method for metallic fibre concrete e measuring the flexural tensile strength (limit of proportionality (LOP), residual), European Committee for Standardization.
Hashash, Y.M., Hook, J.J., Schmidt, B., Yao, J.I.-C., 2001. Seismic design and analysis of underground structures. Tunnell. Underground Space Technol. 16 (4), 247–293.
Kang, T.H.-K., Kim, W., Massone, L.M., Galleguillos, T.A., 2012. Shear-flexure coupling behavior of steel fiber-reinforced concrete beams. ACI Struct. J. 109 (4), 435–444.
Kolymbas, D., 2005. Tunnelling and tunnel mechanics: A rational approach to tunnelling. Springer Science and Business Media.
Kort, I., Musante, H., Fahrenkrog, C., 1979. In situ mechanical properties measurements of gravelly soil used in an interaction and foundation model for the Santiago Metro. In: Proceedings of the 6th Panamerican Conference on Soil Mechanics and Foundation Engineering, Peru, pp. 217–224.
Kuesel, T.R., 1969. Earthquake design criteria for subways. J. Struct. Div. 95 (6), 1213–1231.
Mazzoni, S., McKenna, F., Scott, M.H., Fenves, G.L., 2006. OpenSees command language manual. Pacific Earthquake Engineering Research (PEER) Center.
Möller, S. C., 2006. Tunnel induced settlements and structural forces in linings. Ph.D. Thesis. Univ. Stuttgart, Inst. f. Geotechnik.
Nazar, F., 2016. Analytical and experimental evaluation of the use of polypropylene and steel fibers as reinforcement in shotcrete supports for tunnel interstation of Santiago (in Spanish). Civil engineering thesis. University of Chile.
Nežerka, V., Antoš, J., Sajdlová, T., Tesárek, P., 2016. Use of open source DIC tools for analysis of multiple cracking in fiber-reinforced concrete. Appl. Mech. Mater. 827, 336–339.
Potts, D., 2002. Guidelines for the use of advanced numerical analysis. Thomas Telford.
Taucer, F., Spacone, E., Filippou, F.C., 1991. A fiber beam-column element for seismic response analysis of reinforced concrete structures, vol. 91-17. Earthquake Engineering Research Center, College of Engineering, University of California Berkeley, California.
Wallace, J.W., Elwood, K.J., Massone, L.M., 2008. Investigation of the axial load capacity for lightly reinforced wall piers. J. Struct. Eng.-ASCE 134 (9), 1548–1557.
Wetzig, V., Weiss, R., di Prisco, M., Felicetti, R., Plizzari, G., 2004. Fibre reinforced shotcrete for long tunnel projects in Switzerland. In: 6th International RILEM Symposium on Fibre Reinforced Concretes, RILEM Publications SARL, pp. 545–552.
Yang, Z., Elgamal, A.-W. M., 2000. Numerical modeling of earthquake site response including dilation and liquefaction. Report (Structural Systems Research Project), SSRP-2000/01. University of California at San Diego, Dept. of Structural Engineering.